Probing gravity at cosmic scales

Peirone, S.

Cover Page

The handle http://hdl.handle.net/1887/137440 holds various files of this Leiden University dissertation.

Author: Peirone, S.
Title: Probing gravity at cosmic scales
Issue Date: 2020-10-06

LARGE-SCALE PHENOMENOLOGY OF VIABLE HORNDESKI THEORIES

Ongoing and upcoming cosmological surveys will significantly improve our ability to probe the equation of state of dark energy, $w_{\rm DE}$, and the phenomenology of Large Scale Structure. They will allow us to constrain deviations from the ΛCDM predictions for the relations between the matter density contrast and the weak lensing and the Newtonian potential, described by the functions Σ and μ, respectively. The latter phenomenological functions, also known as $G_{\rm light}/G$ and $G_{\rm matter}/G$, are commonly used to parameterize modifications of the growth of large-scale structure in alternative theories of gravity. In this chapter, we study the values these functions can take in Horndeski theories. We restrict our attention to models that are in a broad agreement with tests of gravity and the observed cosmic expansion history. In particular, we require the speed of gravity to be equal to the speed of light today, as indicated by the recent detection of gravitational waves and electromagnetic emission from a binary neutron star merger, as shown in section 1.4. We examine the correlations between the values of Σ and μ analytically within the quasi static approximation, and numerically, by sampling the space of allowed solutions. In the context of viable Horndeski theories, we confirm the conjecture made in [117] that $(\Sigma - 1)(\mu - 1) \geq 0$ and, we check the validity of the quasi static approximation. Finally, we derive the theoretical prior for the joint covariance of $w_{\rm DE}$, Σ and μ, focusing on the time-dependence at certain representative scales. Our results show that, even with the tight bound on the present day speed of gravitational waves, there is room within Horndeski theories for non-trivial signatures of modified gravity at

the level of linear perturbations and we confirm the high degree of correlation between Σ and μ in scalar-tensor theories. The derived prior covariance matrices will allow us to reconstruct jointly w_{DE}, Σ and μ in a non-parametric way.

3.1   INTRODUCTION

One of the primary goals of ongoing and future surveys of Large Scale Structure (LSS) is testing gravity on cosmological scales and shedding light on the nature of dark energy (DE), *i.e.* the mysterious component thought to be sourcing cosmic acceleration [18, 19, 118]. To this extent, they will provide accurate measurements of the effective equation of state of all non-dust contributions to the Friedmann equation at late times, $w_{DE}(z)$. They will also measure deviations in the phenomenology of LSS from predictions of the standard model of cosmology, ΛCDM. These potential deviations are commonly encoded in the phenomenological functions Σ and μ that parametrize modifications of the perturbed Einstein's equations relating the matter density contrast to the lensing and the Newtonian potential, respectively [119–121].

Constraining functions of redshift and, possibly, scale with data, necessarily involves making assumptions about their properties. Such assumptions can be manifested in a choice of a specific parametric form, which, however, can limit the ability to capture nontrivial features and, more generally, is prone to biasing the outcome. Alternatively, one can reconstruct these functions non-parametrically, *e.g.* by binning them in redshift. As Principal Component Analysis (PCA) studies have shown [122–125], while the upcoming missions can constrain several eigenmodes of $w_{DE}(z)$, $\Sigma(z)$ and $\mu(z)$, many more will remain unconstrained, with values in neighbouring bins effectively being degenerate. A partial lifting of the degeneracy, sufficient to aid the reconstruction, can be achieved by introducing correlations between bins in the form of prior covariances, that can be directly combined with the data co-

variance matrix [126]. While different techniques can be employed to construct these correlation priors [126–131], it is desirable for them to be theoretically informed. In [128] it was derived the theoretical prior covariance matrix for w_{DE} predicted by Horndeski gravity [34–36]. The final aim of this chapter is to extend this work by creating joint theoretical covariance matrices for w_{DE} along with the phenomenological functions Σ and μ: having a (weak) joint prior between them will allow to constrain these functions jointly in a theoretically consistent way, while not biasing the outcome.

In order to fulfil this goal we employ the EFT approach to sample the space of Horndeski theories and create large ensembles of statistically independent models via Monte Carlo techniques. We randomly generate the five EFT functions that enter in the models Lagrangian and we keep those that lead to theoretically consistent and observationally allowed solutions. This means that we require the speed of gravity to be equal to the speed of light today, as recently indicated by the gravitational wave measurement from a neutron star merger [74] and we include constraints on the gravitational coupling, coming from Cosmic Microwave Background (CMB) and Big Bang Nucleosynthesis (BBN) bounds as well as laboratory tests. Furthermore we also impose a weak Gaussian prior on the background expansion history, in order to be broadly consistent with existing cosmological distance measurements. Finally, we impose conditions for the physical viability of the sampled models, mainly avoiding ghost and gradient instabilities of the theory, as introduced in section 1.3.4.

In any specific theory of gravity, the expansion history and the evolution of perturbations follow from the same fundamental Lagrangian and are not independent of each other. Given these prospects, it is pertinent to ask if measuring certain values of these functions could rule out broad classes of modified gravity (MG) theories. For instance, in [117] it was argued that one should expect to have $(\Sigma - 1)(\mu - 1) \geq 0$ in Horndeski theories that are in agreement with the existing observa-

tional and experimental constraints. In principle, mathematically, there is sufficient freedom within the Horndeski class to construct theories that would violate the conjecture. However, according to [117], it would require a specially fine-tuned arrangement of separate sectors of the theory. We can make use of the ensembles of Horndeski model to test such conjecture numerically.

The latter conjecture was based on explicit expressions for Σ and μ derived under the Quasi Static Approximation (QSA). Since our numerical procedure allows us to compute these functions exactly, we verify the validity of the QSA at several representative scales and redshifts. We find that the QSA breaks down at $k \lesssim 0.001$ h/Mpc even though the modes are still well-within the scalar field sound horizon, indicating that the time derivatives of the metric and the scalar field perturbations can no longer be neglected on those scales. Nevertheless, we find that the $(\Sigma - 1)(\mu - 1) \geq 0$ conjecture holds very well on scales probed by large scale structure surveys.

Finally, our simulations allow us to derive several statistical properties of the distributions of w_{DE}, Σ and μ, such as their mean values and distribution functions, in bins of time. Of more practical use (for non-parametric reconstructions), we also obtain their joint covariances and the functional forms of their correlation functions within each subclass of model. We study the dependence of the statistical ensemble on the imposed theoretical priors and mild observational constraints. We also identify trends in the covariances associated to the different sub-classes of theories, such as Generalized Brans-Dicke (GBD), *i.e.* models with a standard form for the scalar kinetic term, and Horndeski models in which the speed of gravity is the same as that of light at all times. Generally, we confirm the high degree of correlation between Σ and μ in scalar-tensor theories.

Our work demonstrates the complementarity of the purely phenomenological Σ and μ parameterization and the EFT approach to testing scalar-tensor theories. The latter can be used to derive the-

oretical priors on Σ and μ, which are more directly constrained by observations.

This chapter is organised as follows: in section 3.2 we review the phenomenological description of cosmological perturbations in Horndeski theories introducing Σ and μ. In section 3.3 we analytically examine the conditions for violating $(\Sigma - 1)(\mu - 1) \geq 0$. In section 3.4 we describe the procedure and in section 3.5 we present the outcome of the numerical sampling of Σ and μ in three representative subclasses of Horndeski theories and the resulting covariance matrices. Finally, in section 3.6 we conclude with a discussion.

3.2 EVOLUTION OF LARGE SCALE STRUCTURE IN HORNDESKI THEORIES

In the Newtonian gauge, scalar perturbations to the Friedmann-Lemaitre-Robertson-Walker (FLRW) metric are the gravitational potentials Ψ and Φ, defined via

$$ds^2 = -(1 + 2\Psi)dt^2 + a^2(1 - 2\Phi)d\mathbf{x}^2, \tag{3.1}$$

where a is the scale factor. The evolution of the metric potentials Φ and Ψ is coupled to that of matter fields through Einsteins' equations. As discussed in [119, 132], non-relativistic particles respond to gradients of Ψ, while relativistic particles "feel" the gradients of the Weyl potential, $(\Phi + \Psi)/2$. In ΛCDM, at epochs when the radiation density can be neglected, one has $(\Phi + \Psi)/2 = \Phi = \Psi$. However, in alternative models, in which additional degrees of freedom can mediate gravitational interactions, the potentials need not be equal. It will be possible to test this by combining the weak lensing shear and galaxy redshift data from surveys like Euclid [133] and LSST [134]. A common practical way

of conducting such tests [121] involves introducing phenomenological functions Σ and μ , defined as

$$k^2(\Phi + \Psi) = -8\pi G\,\Sigma(a,k)\,a^2\rho\Delta \ , \tag{3.2}$$

$$k^2\Psi = -4\pi G\mu(a,k)a^2\rho\Delta \ , \tag{3.3}$$

where ρ is the background matter density and $\Delta = \delta + 3aHv/k$ is the comoving density contrast. Alternatively, one could use any one of the above functions along with the "gravitational slip" [97, 119, 120, 135, 136] $\gamma(a,k)$ defined via $\Phi = \gamma(a,k)\Psi$. As shown in [124, 125], Σ will be well-constrained by the combination of weak lensing and photometric galaxy counts from surveys like Euclid and LSST. Spectroscopic galaxy redshifts will add measurements of redshift space distortions, which probe the Newtonian potential, and will help to measure μ [125, 137, 138]. The parameter γ is not directly probed by cosmological observables but can be derived from the measurement of the other two.

The functions Σ and μ are equal to one in ΛCDM, but generally would be functions of time and the Fourier number k in models beyond ΛCDM. When coupled to the Euler and the continuity equations for matter, eqs. (3.2) and (3.3) form a closed system that can be solved to obtain the phenomenology of LSS on linear scales [121]. Given a functional form of Σ and μ, one can solve for the evolution of cosmological perturbations [121] using, *e.g.* , the publicly available code MGCAMB [139, 140], and constrain these functions by fitting them to data. The question one should then ask is if the measured values of the parameters rule out certain classes of modified gravity models.

Obtaining a closed functional form of Σ and μ in a given gravity theory is only possible under the quasi static (QS) approximation (QSA). The QSA has been shown to hold well in certain representative classes of scalar-tensor theories [54, 56, 141–143]. In [117], the QS expressions for Σ and μ in the Horndeski class of scalar-tensor theories were derived and closely examined. It was observed that there must be correlations

between their values. In particular, one should generally expect to have $\Sigma - 1$ and $\mu - 1$ to be of the same sign in theoretically consistent models that do not grossly contradict observations.

3.2.1   *Background evolution and w_{DE}*

Given the EFT functions $\Omega(a)$ and $\Lambda(a)$ as defined in eq. (1.62), one can use the Friedmann equation to solve for the evolution of the Hubble parameter $\mathcal{H} = a^{-1} da/d\tau$. Namely, introducing $y \equiv \mathcal{H}^2$, we have

$$\left(1 + \Omega + \frac{1}{2}a\Omega'\right)\frac{dy}{d\ln a} + \left(1 + \Omega + 2a\Omega' + a^2\Omega''\right)y$$
$$+ \left(\frac{P_m a^2}{m_0^2} + \frac{\Lambda a^2}{m_0^2}\right) = 0, \qquad (3.4)$$

where the prime indicates differentiation with respect to the scale factor. Given the solution for $\mathcal{H}(a)$, the effective DE equation of state is defined via

$$w_{\text{DE}} \equiv \frac{P_{\text{DE}}}{\rho_{\text{DE}}} = \frac{-2\dot{\mathcal{H}} - \mathcal{H}^2 - P_m a^2/m_0^2}{3\mathcal{H}^2 - \rho_m a^2/m_0^2}, \qquad (3.5)$$

where ρ_m and P_m are the combined energy density and the pressure of all particle species, and the over-dot denotes a derivative with respect to the conformal time. A more detailed description of the background solution is given in [128]. To solve for the perturbations, in addition to Ω and Λ, one needs to specify γ_1, γ_2 and γ_3 multiplying the second order terms in the action. From eq. (1.62), one can work out the full set of linearly perturbed Einstein equations for scalar, vector and tensor modes. Functions Ω and γ_3 affect both scalar and tensor perturbations. In particular, whenever $\gamma_3 \neq 0$, the speed of gravity c_T is different from the speed of light, $c = 1$, making it a key phenomenological signature

of Horndeski gravity. It has become conventional to parameterize this difference as $\alpha_T \equiv c_T^2 - 1$ [47], related to the EFT functions via

$$\alpha_T = -\frac{\gamma_3}{1 + \Omega + \gamma_3} . \tag{3.6}$$

As introduced in 1.4, such deviations have been severely constrained by the recent detection of the neutron star binary GW170817 and its electromagnetic counterpart GRB170817A [61–63], although one must keep two arguments in mind. Firstly, GW170817 is at a distance of 40 Mpc, or $z \sim 0.01$, while cosmological data comes from higher redshifts. So, technically, one can have $\gamma_3 \neq 0$ at $z > 0.01$. Secondly, as pointed out in [78], the GW170817 measurement was performed at energy scales that are close to the cut-off scale at which EFT actions, such as (1.62), become invalid. As explicitly shown in [78] for Horndeski theories, one can have the speed of gravity differ from the speed of light at energy scales relevant for cosmology, but get restored to the speed of light at higher energies due to the terms that dominate near the cutoff scale.

3.2.2 Σ and μ in Horndeski theories

The theoretical expressions for μ and Σ can be derived under the QSA, where one considers the scales below the scalar field sound horizon and ignores the time-derivatives of the scalar field perturbations and the gravitational potentials. In Horndeski theories, they have the form of a ratio of quadratic polynomials in k [117, 144, 145]:

$$\mu = \frac{m_0^2}{M_*^2} \frac{1 + M^2 a^2/k^2}{f_3/2f_1 M_*^2 + M^2(1+\alpha_T)^{-1} a^2/k^2}, \tag{3.7}$$

$$\Sigma = \frac{m_0^2}{2M_*^2} \frac{1 + f_5/f_1 + M^2[1 + (1+\alpha_T)^{-1}] a^2/k^2}{f_3/2f_1 M_*^2 + M^2(1+\alpha_T)^{-1} a^2/k^2}, \tag{3.8}$$

where we defined $M^2 \equiv C_\pi/f_1$ and with the functions C_π, f_1, f_3 and f_5 defined in Appendix 3.8. The mass parameter M sets the scale below

which the scalar field fluctuations contribute a fifth force, *i.e.* , the Compton wavelength $\lambda_C \sim M^{-1}$. Note that, while γ_1 does not enter explicitly in the quasi static expressions for Σ and μ, it still plays a role in determining the stability of perturbations [146].

3.3 THE $(\Sigma - 1)(\mu - 1) \geq 0$ CONJECTURE

In [117], it was conjectured that viable Horndeski models should have

$$(\Sigma - 1)(\mu - 1) \geq 0 . \tag{3.9}$$

Mathematically, there is sufficient freedom in Horndeski theories to violate (3.9). The conjecture is such that violations are unlikely, because they require balancing the evolution of the background gravitational coupling, *i.e.* the m_0^2/M_*^2 pre-factor in Eqs. (3.7)-(3.16), with the change in the speed of gravity waves (α_T) and the fifth force contribution, quantified by β_B and β_ξ, in a rather special way. A statement about the likeliness of something occurring necessarily depends on the choice of the priors. In this instance, the key assumption is that the dynamics of both the background and the perturbations are derived from the same Lagrangian, which can be of any form consistent with (1.59). For instance, one could imaging constructing an ensemble of Horndeski theories by randomly sampling all functions of ϕ and X appearing in (1.59), along with all possible initial conditions. Since an evolving gravitational coupling affects both the expansion rate and the fifth force contribution, restricting to the subset of solutions with an acceptable $H(a)$ reduces the probability of achieving the fine-tuning necessary to violate (3.9).

In practice, sampling the action (1.59) directly would be prohibitively costly without making significant simplifying assumptions (*e.g.* see [72]). Another option, given that we are only interested in the background and linear perturbations, is to work with (1.62) and sample the EFT functions, treating them as being *a priori* independent. Since

functions Ω and Λ (and c, which can be derived from them) in (1.62) affect the background evolution, *a posteriori* restrictions on $H(a)$ will constrain variations in $\Omega(a)$, which is the EFT function controlling the evolution of the gravitational coupling, making it harder to violate the conjecture (3.9). This effect would be absent had we assumed that $H(a)$ was known *a priori*, which is the case if one samples the action (1.64) instead, where $H(a)$ is assumed to be known independently from $M_*^2(a)$, α_B, α_K and α_T. The probability of seeing exceptions to (3.9) is further lowered by constraints on the variation of the gravitational coupling from the big bang nucleosynthesis (BBN), CMB and various fifth force bounds [147], and the strict bound on the speed of gravitational waves imposed by GW170817 and GRB170817A [61–63].

In the remainder of this section, we analytically examine the conditions under which (3.9) can be violated, separately considering the limiting cases of the super- and sub-Compton scales. It is reasonable to expect the cosmological observational window to fall into one of these limits, since the Compton wavelength is either very large ($\lambda_C \sim H^{-1}$) in models of self-accelerating type [141], or very small ($\lambda_C < 1$ Mpc) in models of chameleon type [148–156]. The exact solutions can be studied numerically and are presented in Section 3.4. As mentioned above, in scalar-tensor theories there is a scale, connected to the scalar field's Compton wavelength, that defines the range of the fifth force, which is suppressed on scales above λ_C. From (3.8) we can identify this scale with the M^2 term, which sets the transition scale of the phenomenological functions: thus when $k/a \ll M$ we are in the large scales (or super-Compton) limit, while, when $k/a \gg M$ we are in the small scales (or sub-Compton) limit.

3.3.1 *The super-Compton limit*

In the $k/a \ll M$ limit, corresponding to scales above the Compton wavelength, (3.7) and (3.8) reduce to

$$\mu_0 = \frac{m_0^2}{M_*^2}(1 + \alpha_T), \tag{3.10}$$

$$\Sigma_0 = \frac{m_0^2}{M_*^2}\left(1 + \frac{\alpha_T}{2}\right). \tag{3.11}$$

This implies that the gravitational slip on super-Compton scales is determined solely by the speed of gravitational waves [117], *i.e.*

$$\gamma_0 = \frac{1}{1 + \alpha_T} = c_T^{-2}. \tag{3.12}$$

The condition to have $\mu_0 > 1$ and $\Sigma_0 < 1$ can be written as

$$(1 + \alpha_T)(1 + \frac{1}{2}\alpha_T) < \Omega < (1 + \alpha_T)^2, \tag{3.13}$$

where we have used Eqs. (3.50) and (3.52) to express M_*^2 in (3.11) in terms of Ω and α_T. A necessary condition for (3.13) to hold is $\alpha_T > 0$, which implies $\Omega > 1$. Similarly, to have $\mu_0 < 1$ and $\Sigma_0 > 1$, we must have

$$(1 + \alpha_T)^2 < \Omega < (1 + \alpha_T)(1 + \frac{1}{2}\alpha_T), \tag{3.14}$$

which requires $\alpha_T < 0$ and, hence, $\Omega < 1$. The conditions (3.13) and (3.14) imply that, to have an observable violation of (3.9), there has to be a significant $\alpha_T \neq 0$ and a corresponding $\Omega \neq 1$, both of which are constrained to be close to their GR values today [157–159]. While GW170817 and GRB170817A [61–63] require α_T to vanish at $z < 0.01$, in principle, there are no observational bounds on α_T at high redshifts. On the other hand, Ω is constrained to be within 10% of its today's value

during the BBN epoch and at the last scattering [147]. Also, $\dot{\Omega} \neq 0$ implies a new interaction between massive particles mediated by the scalar field, which is constrained by probes of structure formation. Thus, it would be challenging to arrange for (3.9) to be violated on super-Compton scales, *and* be observable.

3.3.2 *The sub-Compton limit*

On scales below the Compton wavelength, *i.e.* in the limit $k/a \gg M$, the expressions for μ and Σ become

$$\mu_\infty = \frac{m_0^2}{M_*^2}(1 + \alpha_T + \beta_\xi^2), \tag{3.15}$$

$$\Sigma_\infty = \frac{m_0^2}{M_*^2}\left(1 + \frac{\alpha_T}{2} + \frac{\beta_\xi^2 + \beta_B\beta_\xi}{2}\right). \tag{3.16}$$

where, following [49][1], we defined

$$\beta_B = -\sqrt{\frac{2}{c_s^2\alpha}}\frac{\alpha_B}{2} \tag{3.17}$$

$$\beta_\xi = \sqrt{\frac{2}{c_s^2\alpha}}\left[-\frac{\alpha_B}{2}(1 + \alpha_T) + \alpha_T - \alpha_M\right] \tag{3.18}$$

$$\alpha = \alpha_K + \frac{3}{2}\alpha_B^2, \tag{3.19}$$

with the expression for the speed of sound of the scalar field perturbations, c_s^2, given by Eq. (3.61) in Appendix 3.8. Stability of linear perturbations requires $\alpha > 0$ and $c_s^2 > 0$ [47, 160].

The condition to have $\mu > 1$ and $\Sigma < 1$ is

$$1 + \frac{1}{2}(\alpha_T + \beta_\xi^2 + \beta_\xi\beta_B) < \frac{\Omega}{1 + \alpha_T} < 1 + \alpha_T + \beta_\xi^2, \tag{3.20}$$

---

1 The definition of α_B in [49] differs from that in [47] by a factor of -2. We use the original definition of [47].

while, to have $\mu < 1$ and $\Sigma > 1$, we must have

$$1 + \alpha_T + \beta_\xi^2 < \frac{\Omega}{1 + \alpha_T} < 1 + \frac{1}{2}(\alpha_T + \beta_\xi^2 + \beta_\xi \beta_B) \,. \tag{3.21}$$

The argument made in [117] was that it would take significant fine-tuning to arrange for the background (Ω, α_T) contributions to μ and Σ to balance the fifth force (β_ξ, β_B) contributions in a precise way to satisfy conditions (3.20) or (3.21).

To gain insight into the degree of fine-tuning involved in satisfying conditions (3.20) or (3.21), we next examine the subclass of theories with $\alpha_T = 0$. Such theories are simpler to analyze and are favored by the recent bounds from GW170817 and GRB170817A [61–63].

3.3.3 *Theories with unmodified speed of gravitational waves*

We will refer to the sub-class of Horndeski theories with the speed of gravity equal to the speed of light as H_S. The change in the gravity speed is given by α_T, related to EFT functions via

$$\alpha_T = -\bar{M}_2^2 / M_*^2 \,. \tag{3.22}$$

Setting $\bar{M}_2^2 = 0$ within the EFT framework ensures $\alpha_T = 0$. In terms of the functions in the Horndeski Lagrangian, α_T is given by [47]

$$\alpha_T = 2X[2G_{4X} - 2G_{5\phi} - (\ddot{\phi} - H\dot{\phi})G_{5X}]M_*^{-2} \,. \tag{3.23}$$

Thus, requiring $\alpha_T = 0$ implies $G_{4X} = G_{5X} = G_{5\phi} = 0$ as discussed in [117] and more recently in [68, 70].

In H_S, the non-trivial EFT functions are Ω, Λ, c, M_2^4 and $\bar{M}_1^3$. Using the relations (3.50)- (3.54), we can write

$$M_*^2 = m_0^2 \Omega \tag{3.24}$$

$$\alpha_M = \frac{\dot{\Omega}}{H\Omega} \tag{3.25}$$

$$\alpha_B = -\frac{\dot{\Omega}}{H\Omega} - \frac{\bar{M}_1^3}{Hm_0^2\Omega} = -\alpha_M - g_3, \tag{3.26}$$

where we have introduced

$$g_3 \equiv \frac{\bar{M}_1^3}{Hm_0^2\Omega} \ . \tag{3.27}$$

Then,

$$\beta_B = \sqrt{\frac{2}{c_s^2\alpha}} \frac{\alpha_M + g_3}{2} \tag{3.28}$$

$$\beta_\xi = \sqrt{\frac{2}{c_s^2\alpha}} \left[\frac{g_3 - \alpha_M}{2}\right] . \tag{3.29}$$

Substituting these expressions into Eqs. (3.15) and (3.16), we get

$$\mu_\infty = \frac{1}{\Omega} \left[1 + \nu(\alpha_M - g_3)^2\right] , \tag{3.30}$$

and

$$\Sigma_\infty = \frac{1}{\Omega} \left[1 + \nu(\alpha_M - g_3)^2 + \nu(\alpha_M g_3 - \alpha_M^2)\right]$$
$$= \mu_\infty + \frac{\nu}{\Omega}(\alpha_M g_3 - \alpha_M^2) , \tag{3.31}$$

where we have defined $\nu \equiv (2c_s^2\alpha)^{-1}$. Conditions (3.20) and (3.21) become

$$1 + \nu(g_3^2 - \alpha_M g_3) < \Omega < 1 + \nu(\alpha_M - g_3)^2 \tag{3.32}$$

and

$$1 + \nu(\alpha_M - g_3)^2 < \Omega < 1 + \nu(g_3^2 - \alpha_M g_3). \tag{3.33}$$

In addition, stability conditions require $c_s^2 \alpha \geq 0$, hence ν cannot be negative.

At this point, we can make two observations:

1. Neither (3.32) nor (3.33) can be satisfied if $\alpha_M \propto \dot{\Omega} = 0$. Thus, violating the conjecture generally requires a notable variation of the background gravitational coupling, which is observationally constrained [147];

2. Condition (3.33) cannot be satisfied if $g_3 = 0$, implying that $\mu < 1$ and $\Sigma > 1$ cannot happen in models with a canonical form of the scalar field kinetic energy term, *i. e.* models of the generalized Brans-Dicke (GBD) type.

To gain further insight, let us consider conditions (3.32) and (3.33) separately.

3.3.3.1   *Conditions for having $\mu > 1$ and $\Sigma < 1$*

Since ν is non-negative, a necessary condition for (3.32) to hold is $(\alpha_M - g_3)^2 > (g_3^2 - \alpha_M g_3)$, or

$$\alpha_M^2 > \alpha_M g_3, \tag{3.34}$$

which is automatically satisfied if α_M and g_3 have opposite signs. In principle, there is nothing prohibiting this from happening. However, observational constraints on Ω and $\alpha_M \propto \dot{\Omega}$, as well as constraints on $H(a)$ which also limit variations of $\Omega(a)$, will generally suppress large departures from GR with $\mu > 1$ and $\Sigma < 1$. This is, in fact, what we see in our simulations, comparing the results before and after the observational constraints are applied.

3.3.3.2   *Conditions for having $\mu < 1$ and $\Sigma > 1$*

Requiring stability of perturbations plays an important role in eliminating solutions with $\mu < 1$ and $\Sigma > 1$. Stability ensures that the force mediated by the scalar field fluctuations is attractive, thus increasing the value of the effective Newton's constant. The only way to arrange for $\mu < 1$ is by making $\Omega > 1$. But Ω is constrained to be close to unity today [23, 142, 161], which means it would be very difficult to detect $\mu < 1$ at low redshifts. Having $\Omega > 1$ would also tend to make $\Sigma < 1$, unless the fifth force contribution to Σ is large enough to make $\Sigma > 1$, while still being small enough to keep $\mu < 1$, which is hard to arrange.

Mathematically, a necessary condition for (3.33) to hold is $(\alpha_M - g_3)^2 < (g_3^2 - \alpha_M g_3)$, or

$$\alpha_M^2 < \alpha_M g_3 . \tag{3.35}$$

This is satisfied only if α_M and g_3 are of the same sign and $\alpha_M^2 < g_3^2$. On the other hand, stability of perturbations requires $c_s^2 \alpha > 0$, which, for H_S, can be written as

$$
\begin{aligned}
c_s^2 \alpha = (\alpha_M^2 - g_3^2) + 2(\alpha_M - g_3) - \frac{2\dot{H}}{H^2}(2 + \alpha_M + g_3) \\
- \frac{1}{H}(\dot{\alpha}_M + \dot{g}_3) - \frac{\rho_m + P_m}{M_*^2 H^2} > 0.
\end{aligned}
\tag{3.36}
$$

Note that $\alpha_M^2 < g_3^2$ makes the first term on the right hand side of (3.36) strictly negative, while the other terms could still be of either sign. Now, imagine sampling α_M and g_3 from a distribution centered around 0. The strictly negative first term would skew $c_s^2 \alpha$ towards negative values, reducing the probability of simultaneously satisfying (3.35) and (3.36). In the next Section, we numerically confirm that imposing the stability condition practically eliminates the solutions with $\mu < 1$ and $\Sigma > 1$.

3.4 METHODOLOGY: THE ENSEMBLE OF μ AND Σ IN HORNDESKI THEORIES

In our analysis, we will scan the theory space of Horndeski gravity by considering several representative combinations of EFT functions Ω, Λ, γ_1, γ_2 and γ_3, with their time dependence drawn from a general ensemble. Specifically, we will consider three families of scalar-tensor theories:

- Generalized Brans Dicke (GBD) models, *i.e.* theories with a standard kinetic term for the scalar field. Jordan Brans-Dicke [162] and $f(R)$ [151] models are representatives of this class. Within the EFT framework, they require specifying two functions, Λ and Ω.

- H_S: the subclass of theories in which the speed of gravity is the same as the speed of light. The H_S class includes GBD models, and allows for non-canonical forms of the kinetic term for the scalar field but without the higher derivative couplings. Kinetic Gravity Braiding (KGB) [107] is an example of such models. In the EFT language, it is described by four functions: Λ, Ω, γ_1 and γ_2. We call this class of theories H_S because it contains all Horndeski models in which the modifications with respect to ΛCDM are solely in the scalar (hence "S") sector (up to the modification of the friction term in the tensor equations from the non-minimal coupling).

- Horndeski (Hor): refers to the entire class of scalar-tensor theories with second order equations of motion [34]. It includes all terms in the action (1.62) specified by functions: Λ, Ω, γ_1, γ_2 and γ_3. In Hor, the speed of gravity can be different from the speed of light, but we only allow such deviations at earlier epochs, requiring that $\gamma_3 = 0$ today to satisfy the constraint coming from the recent

detection of gravitational waves from a neutron star binary along with the electromagnetic counterpart [62, 163, 164].

The above classes of theories, and the associated EFT functions, are summarized in Table 3.1.

In order to scan the theory space, we have adopted the numerical framework developed in [128]. It consists of a Monte Carlo (MC) code which samples the space of the EFT functions, building a statistically significant ensemble of viable models. For each model, it computes and stores the values of w_{DE}, Σ and μ at densely spaced values of redshifts.

To build the samples, we parametrize the EFT functions using a Padé expansion of order $[M, N]$, *e.g.*

$$f(a) = \frac{\sum_{n=1}^{N} \alpha_n (a - a_0)^{n-1}}{1 + \sum_{m=1}^{M} \beta_m (a - a_0)^{m}} .$$ (3.37)

We use expansions around $a_0 = 0$ and $a_0 = 1$, to represent models that are close to ΛCDM in the past (*thawing*) or at present (*freezing*), respectively. Since the acceptance rate is different in each case, the desired sample size is not reached after the same number of sampled models, leading to a different respective statistical significance. We address this by re-weighting the samples based on the respective acceptance rate when processing the data.

The MC sampler varies the coefficients α_n and β_m in the range $[-1, 1]$. We have investigated using broader ranges, such as $[-10, 10]$ and $[-50, 50]$, and found that it did not noticeably increase the ensemble of viable models. We attribute this to the fact that models with larger departures from ΛCDM are less likely to satisfy the stability constraints described below. We fix the spatial curvature to be zero, take the sum of neutrino masses to be 0.06 eV, and impose conservative priors on the relevant cosmological parameters. Namely, the matter density fraction is allowed to change in the range $\Omega_m \in [0, 1]$. Similarly, the present day dark energy fraction, which is not fixed by the flatness condition in non-minimally coupled models, was allowed to span $\Omega_{\text{DE}} \in [0, 1]$.

Name	Lagrangian functions in (1.59)
GBD	$K = X - V(\phi), G_4 = G_4(\phi)$
H_S	$K(X, \phi), G_3(X, \phi), G_4 = G_4(\phi)$
Horndeski	$K(X, \phi),\ G_i(X, \phi),\ i = 3, 4, 5$

	"EFT" functions in (1.62)
GBD	Ω, Λ
H_S	$\Omega, \Lambda, \bar{M}_1^3, M_2^4$
Horndeski	$\Omega, \Lambda, \bar{M}_1^3, M_2^4, \bar{M}_2^2(z = 0) = 0$

	"Unified" functions in (1.64)
GBD	$H, \alpha_B = -\alpha_M, \alpha_K$
H_S	$H, \alpha_B, \alpha_M, \alpha_K$
Horndeski	$H, \alpha_B, \alpha_M, \alpha_K, \alpha_T(z = 0) = 0$

Table 3.1: The three sub-classes of Horndeski theories considered in Section 3.4, defined in alternative but equivalent ways.

Summarising, the parameters varied in the MCMC analysis are α_n, β_m, Ω_m, Ω_{DE} and H_0.

To compute the background evolution for a given model, the sampler was interfaced with the Einstein-Boltzmann solver EFTCAMB.

Given a choice of EFT functions, EFTCAMB first solves for the background evolution, then checks if conditions ensuring the stability of linear perturbations are satisfied, and then evolves such perturbations to evaluate the CMB spectra and other observables. Given the exact solutions for Δ, Φ and Ψ for a given model in the ensemble, we can calculate the exact $\mu(a,k)$ and $\Sigma(a,k)$ from Eqs. (3.3) and (3.2) that define them. Alternatively, we can use EFTCAMB to perform the first two stages, *i.e.* to evolve the background and perform the stability check, and then evaluate Σ and μ using the quasi static (QS) expressions (3.7) and (3.8). For each sampling, we will present the results for the exact and the QS (μ, Σ). By doing it both ways we can assess the validity of the QSA within Horndeski and also test the analytical arguments made in the previous Section under the QSA.

In order for a model to be accepted by the sampler, it has to pass several checks. First, the model has to pass the stability conditions, as built in EFTCAMB. This filters out models with ghost and gradient instabilities in the scalar and tensor sectors. Further, we require viable models to fulfil weak observational and experimental priors on $\alpha_T(a)$, $\Omega(a)$ and $H(a)$. We emphasize that it is not our aim to perform a fit to data to derive observational bounds on Σ and μ. Instead, we want to derive theoretical priors on their values, but we want to exclude models that are in a gross violation of known constraints. The following priors simply require the realizations to be broadly acceptable:

- $\alpha_T(z = 0) = 0$, to be consistent with the low redshift bounds on the speed of gravitational waves from GW170817 and GRB170817A [61–63];

- $|\Omega(z = 0) - 1| < 0.1$, to be broadly consistent with the non-detection of the fifth force on Earth [23, 142, 161];

- $|\Omega(z = 1100) - 1| < 0.1$, to comply with the BBN and CMB bounds constraining the value of the gravitational coupling to be within 10% of the Newton's constant measured on Earth [147];

- $H(z)$ to be broadly consistent with existing cosmological distance measurements (see below for more details).

To dismiss expansion histories that are in gross disagreement with observations, we impose a weak Gaussian prior on $H(z)$ at several representative redshift values corresponding to existing luminosity distance measurements from supernovae and angular diameter distance measurements using Baryon Acoustic Oscillations (BAO). We take the prior to be peaked at $H(z)$ derived from the Planck 2015 best fit ΛCDM model [114], with the standard deviation set at 30% of the peak value. The width of the prior is deliberately chosen to be wide enough to accommodate any tension existing between different datasets [129]. The peak values of the $H(z)$ prior, along with the standard deviation, are plotted in figure 3.1.

We then proceed with the MC sampling: the coefficients of the EFT functions, as defined in (3.37), vary at each step. This ensures that we get numerical results that go through the whole parameter space homogeneously. To ensure a good coverage, we enforce a minimum number of 10^4 accepted Monte Carlo samples. Depending on the acceptance rate, this results in total of $\sim 10^6 - 10^8$ samples.

At each Monte Carlo step, after solving the background equations, we evaluate the stability of the corresponding model and, if this is found stable we compute the values of $w_{\text{DE}}(a)$, $\Sigma(a, k)$ and $\mu(a, k)$. n order to study the validity of the conjecture (3.9) we decide to store the
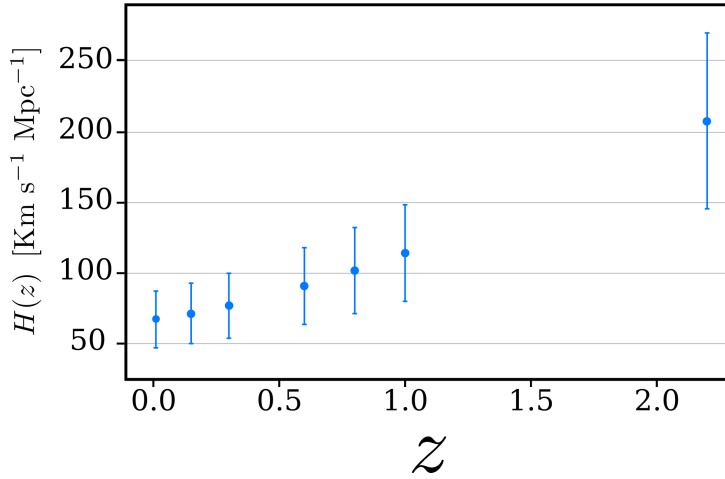
Figure 3.1: The peak values and the standard deviation of the Gaussian prior imposed on the evolution of the Hubble parameter, $H(z)$. The fiducial expansion history corresponds to the Planck 2015 best fit ΛCDM model [114]. The standard deviation is chosen to be wide enough to accommodate any tensions that may exist between different datasets.

values of Σ and μ, both QS and exact, sampling the (a, k)-plane at the following values:

$$a \in \{0.25, 0.575, 0.9\},$$
$$k \in \{0.001, 0.05, 0.1\},$$

where k has units of h/Mpc. By considering the three different classes of theories in Table 3.1 we are then able to study the effect of different EFT functions on the distribution of Σ and μ.

3.4.1 *Covariance matrices*

The final aim of this work is to provide theoretical prior distributions of bins of $w_{\mathrm{DE}}(z)$, $\Sigma(z)$ and $\mu(z)$ that can be used in their joint recon-

struction from data. Gaussian prior distributions can be built from the mean values and covariances of the bins obtained using the MC method described in the previous Section. As presented below, we have derived them separately for the three representative subclasses of Horndeski theories. The actual values of the means and the exact shapes of the prior distributions are not crucial in the Bayesian reconstruction method of [126]. The role of the prior is to gently guide the reconstruction in regions of the parameter space poorly constrained by data. For this reason, we also derive the approximate analytical forms describing the correlation between the bins that can be readily applied in practical applications without a loss of accuracy. We then run a second set of simulations keeping the fix value $k = 0.01\ h\ \mathrm{Mpc}^{-1}$, which, as we will see in the following section, ensures that linear theory holds well and the QSA is valid. We store $w_{\mathrm{DE}}(a)$, $\Sigma(a)$ and $\mu(a)$ at 100 uniformly spaced values of $a \in [0.1, 1]$, which corresponds to $z \in [0, 9]$. Given these ensembles, we compute the mean values and the covariance matrices of the $w_{\mathrm{DE}}(a)$, $\Sigma(a)$ and $\mu(a)$ bins. The covariance matrix is defined as

$$C_{ij} = \frac{1}{N_{\mathrm{samp}} - 1} \sum_{k=1}^{N_{\mathrm{samp}}} \left(x_i^{(k)} - \bar{x}_i \right) \left(x_j^{(k)} - \bar{x}_j \right),\tag{3.38}$$

where $x_i^{(k)} = x^{(k)}(z_i)$, $\bar{x}_i$ is the mean value of x in the i-th redshift bin, and k labels a member of the sample of N_{samp} models in the ensemble. The prior covariance matrices, along with the mean values, can be used to build a Gaussian prior probability distribution function that can be used to reconstruct [126] functions $w_{\mathrm{DE}}(a)$, $\Sigma(a)$ and $\mu(a)$ from data, as was done for $w_{\mathrm{DE}}(a)$ in [127, 129]. One can also define the normalized correlation matrix as

$$\mathcal{C}_{ij} = \frac{C_{ij}}{\sqrt{C_{ii}C_{jj}}}.\tag{3.39}$$

For practical applications, it can be useful to have analytical expressions for the continuous correlation function defined as

$$C(a, a') \equiv \langle [x(a) - \bar{x}(a)][x(a) - \bar{x}(a')] \rangle . \qquad (3.40)$$

We will derive them by fitting representative functional forms to (3.39).

3.5   RESULTS OF THE NUMERICAL SAMPLING

3.5.1   *Numerical study of the conjecture*

Figures 3.2, 3.3 and 3.4 show the numerically sampled distributions of Σ and μ at representative values of a and k for GBD, H_S and the full Horndeski model with the speed of gravity constrained to be unmodified today. In each figure, for the same ensemble of models, we show both the "exact" values, (calculated by numerically solving the full set of equations governing cosmological perturbations), as well as the values obtained using the QS expressions for Σ and μ given by Eqs. (3.7) and (3.8). We find that for all three models the QSA holds extremely well at $k = 0.1$ and 0.05 h/Mpc. Indeed, the clouds of exact and QS points effectively coincide for GBD and H_S, while for Horndeski there are only a few minor differences. We also see that, at $k = 0.1$, 0.05 h/Mpc and at all redshifts, $\Sigma - 1$ and $\mu - 1$ are almost always of the same sign, following the conjecture made in [117].

We notice that at these scales we do not find any significant dependence on k. This is because the sampled models tend to have a mass scale $M \sim H$, and thus the mass term has no effect on scales inside the horizon. In principle, one could also find models where $M \gg H$, but that would require a taylored sampling strategy, as this class of models is of measure zero in our framework. Models with $M \gg H$ include $f(R)$ and other chameleon type theories, which can be tested directly using simpler techniques.
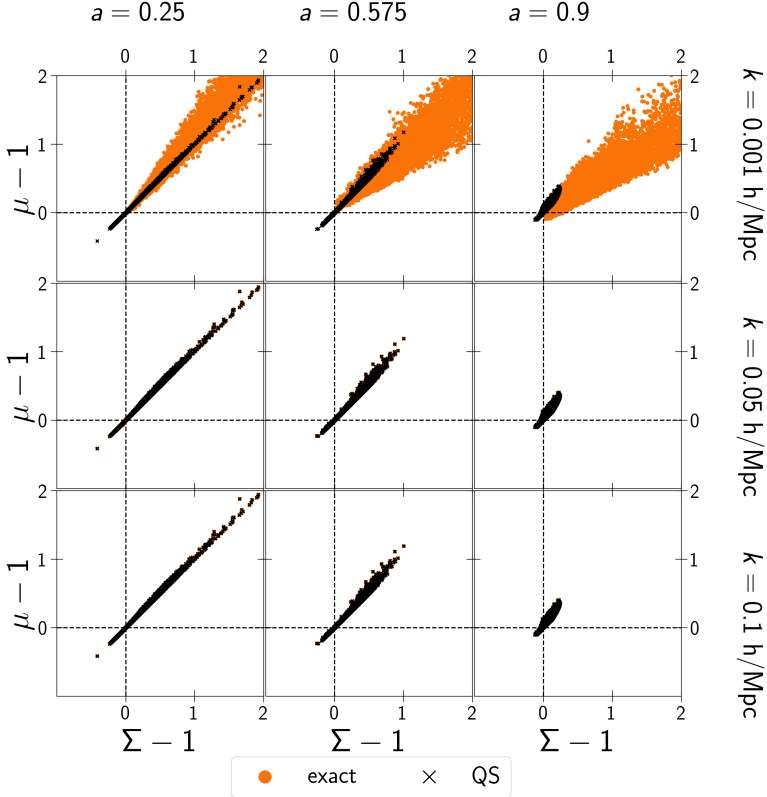
Figure 3.2: Distributions of Σ and μ in GBD models, *i.e.* the scalar-tensor models with a canonical kinetic term, at representative values of a and k. Shown are results obtained by numerically solving exact equations for cosmological perturbations (orange dots) and by using the quasi static (black crosses) forms of Σ and μ given by Eqs. (3.7) and (3.8).
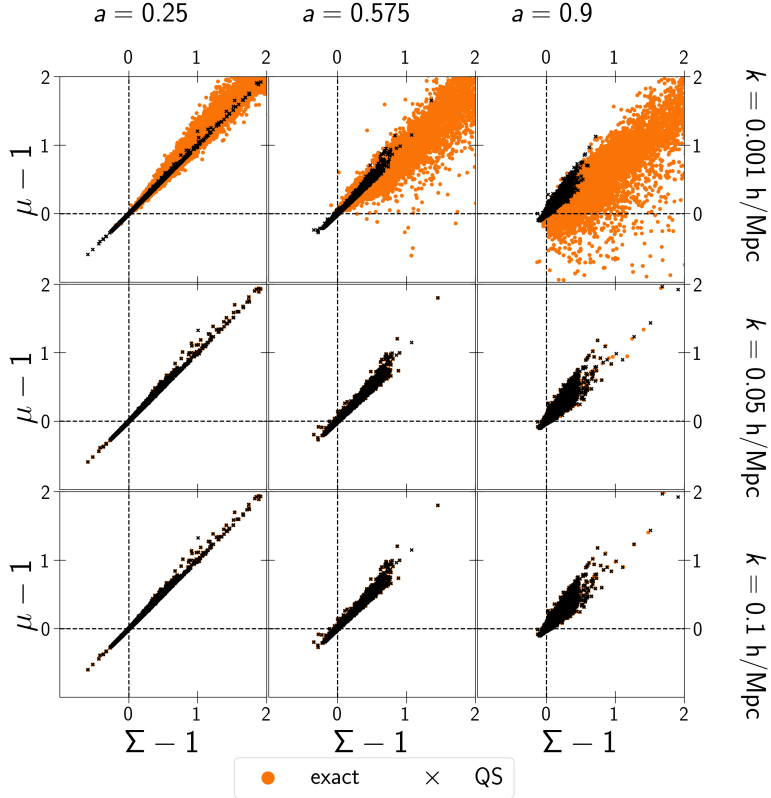
Figure 3.3: Same as in figure 3.2 but for the H_S models, *i.e.* the subset of Horndeski models in which the speed of gravitational waves is the same as the speed of light at all redshifts.
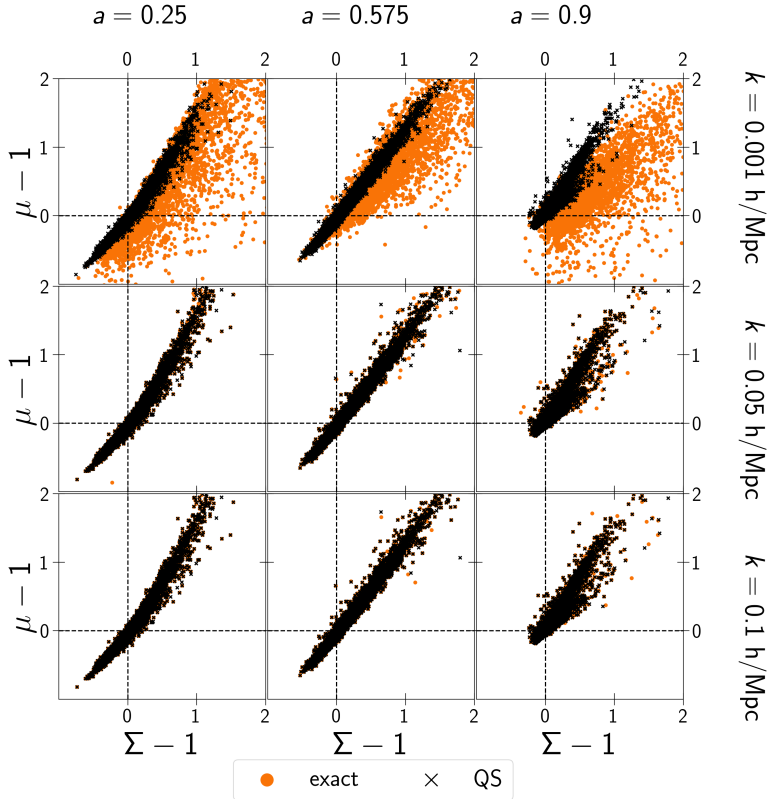
Figure 3.4: Same as in figures 3.2 and 3.3, but for the full class of Horndeski models with the restriction on variation of the speed of gravitational waves imposed only at $z = 0$.
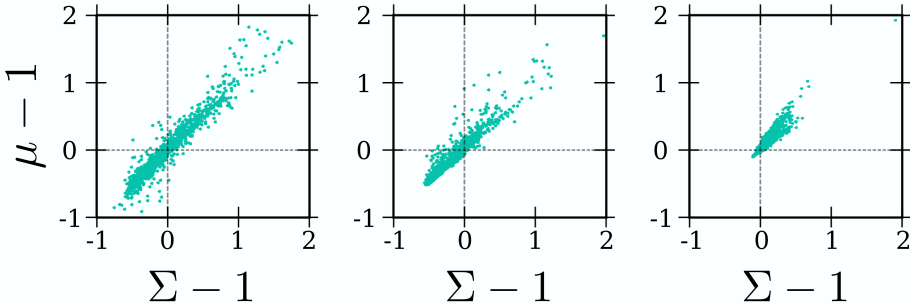
Figure 3.5: Effects of imposing the stability conditions and observational priors on the Σ-μ distribution in the H_S model for $a = 0.9$ and $k = 0.1$ h/Mpc. The three panels correspond to samples obtained in three different runs: sampling without any constraints (left panel), sampling with the stability constraints (middle), and sampling with both the stability constraints and observational priors (right). Each panel contains 10^4 points. The impacts of stability and observational constraints shown here are representative of what happens at other redshifts and scales, and in the other classes of models that we studied.

The agreement between the exact and the QS calculations is much worse at $k = 0.001$ h/Mpc, where we can see that the clouds of exact points are more spread compared to the QS clouds. A necessary condition for the QSA to hold is the requirement for the given Fourier mode to be inside the scalar field's sound horizon, *i.e.*

$$\frac{k}{aH(a)} > c_s(a) \, , \tag{3.41}$$

where the speed of sound is given by Eq. (3.61). In addition, the QSA assumes that the time-derivatives of the gravitational potentials and the scalar field perturbations are negligible compared to the spatial derivatives. To isolate the reason for the breakdown of the QSA at $k = 0.001$ h/Mpc, we checked the fraction of models that pass the necessary condition (3.41) and found that only 1% out of the total sample of 10^4 models failed it. This implies that for $k \lesssim 0.001$ h/Mpc

one can no longer neglect the time-derivatives of the metric and field perturbations even on scales within the sound horizon of the scalar field.

In the case of GBD, as seen in figure 3.2, the majority of both the QS and the exact values satisfy $(\Sigma - 1)(\mu - 1) \geq 0$. Only about 1% of exact points in the $k = 0.001$ h/Mpc, $a = 0.9$ panel violate the conjecture, with no violations seen in the other panels. For H_S, the conjecture holds very well for the QS points, but not always for the exact points. We find that about 10% of the exactly calculated points fall in the bottom-right quadrant at late redshifts and large scales, i.e. in the $k = 0.001$ h/Mpc, $a = 0.9$ panel, with only a handful of points violating the conjecture at higher redshifts for $k = 0.001$ h/Mpc. Finally, for the full Horndeski sampling, we again find that the conjecture holds well under the QSA, and for the exact points on smaller scales ($k = 0.1$ and 0.05 h/Mpc). However, about 10% of the models violate the conjecture at all three values of a for $k = 0.001$ h/Mpc. It is interesting to notice that, in those cases, the conjecture is always violated in the same direction, with a positive $\Sigma - 1$ and a negative $\mu - 1$.

In figure 3.5, we show the effects of imposing the stability constraints and observational priors on the distribution of Σ and μ. We consider the case of the H_S model at $k = 0.1$ h/Mpc and $a = 0.9$, which is representative of the trends we see at other scales and redshifts and in the other models. The three panels show samples of the H_S models without imposing any constraints (left panel), after filtering out models with the ghost and gradient instabilities [160] (middle panel) and after imposing both the stability constraints and observational priors (right panel). In each case, we run the simulation until 10^4 "successful" models are accumulated. From these plots, we can see that imposing the stability conditions removes all points from the bottom-right quadrant. As discussed in Section 3.3.3.2, this happens because stability requires $c_s^2 \alpha > 0$. Finally, in the right panel, we see that adding the observational priors eliminates the models belonging to the top-left quadrant. This

confirms the argument made in Section 3.3.3.1 according to which getting $\Sigma < 1$ and $\mu > 1$ would require large variations in Ω, which are indeed strongly suppressed by the observational constraints defined in the beginning of this Section. We note that the points in the middle and the right panels are not simple subsets of the left panel, since we run the simulation until the same number of points is accumulated in each case.

From figure 3.5 we also notice that the combined effect of the stability conditions and the observational priors is to drastically reduce the models in the bottom-left quadrant, where $\mu - 1 < 0$ and $\Sigma - 1 < 0$. In the absence of ghosts, the scalar force is always attractive, thus the fifth force contribution generally favours $\mu > 1$. One could still have $\mu < 1$, driven by the $1/\Omega$ factor in the QS expression (3.30) for μ, *i.e.* having Ω that is significantly greater than 1 can result in $\mu < 1$. However, observational constraints restrict $\Omega \sim 1$ at late times, making it difficult to get $\mu < 1$. We see in figure 3.3 that the bottom-left quadrant has practically no points at $a = 0.9$, but is more populated at earlier times, since the observational constraint on Ω are weaker at higher redshifts.

3.5.2 *The mean values of w_{DE}, Σ and μ*

The mean values of $w_{\mathrm{DE}}(z)$, $\Sigma(z)$ and $\mu(z)$ bins, along with the corresponding 68%, 95% and 99% confidence level intervals, are shown in figure 3.6.

We observe that the mean values of Σ and μ do not change significantly with redshift, and that for H_S and Hor models they always remain within $\sim 1\sigma$ range of their ΛCDM values of 1. For GBD, the ΛCDM values remain in the 2σ range, with a clear trend towards values below 1. This is because, in GBD, the values of Σ and μ are largely determined by the prefactor $m_0^2/M_*^2 = 1/(1 + \Omega)$ multiplying them both. Given a uniformly sampled Ω, this prefactor is likely to be < 1, because $1 + \Omega$ must remain positive to guarantee the stability of the
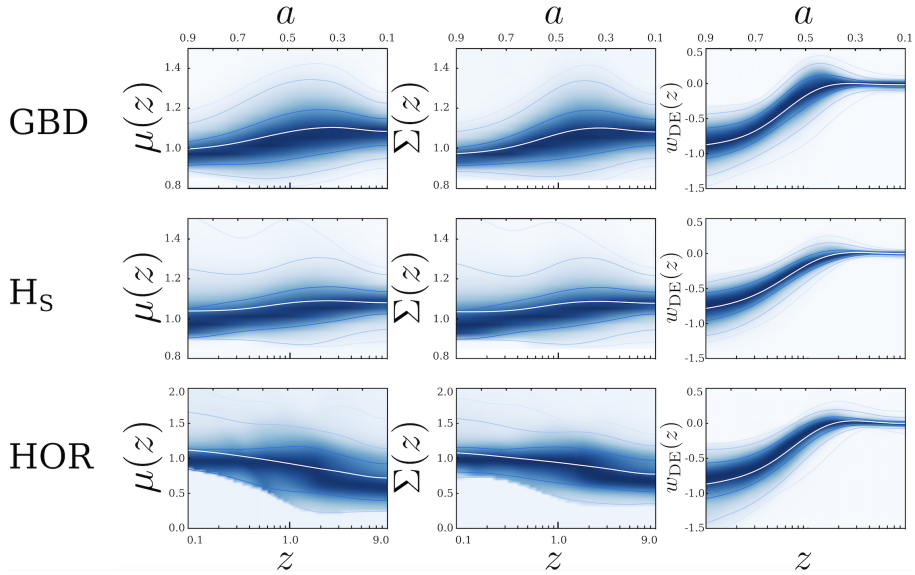
Figure 3.6: The mean values (white line) and the 68%, 95% and 99% confidence levels (solid blue lines) for $\mu(z)$, $\Sigma(z)$ and $w_{\text{DE}}(z)$ (left to right respectively) for the three classes of models: GBD (top row), H_S (middle row) and Horndeski (bottom row). The shaded blue regions represent the probability distribution function (PDF) of each bin.

background solution, hence values of $\Omega \sim -1$ are often rejected by the stability filters built into the sampler. We note that, ultimately, the mean values should not play a significant role in practical applications. The uncertainties in the mean values are more relevant as they are linked to the covariances between w_{DE}, Σ and μ bins. Nevertheless, one does need some values to put in the Gaussian prior, and it is interesting to see what one gets from the ensembles.

In the case of $w_{\mathrm{DE}}(z)$, the means are close to the ΛCDM value of $w_{\mathrm{DE}} = -1$ at lower redshifts, where the SN data plays a role. At higher redshifts, $w_{\mathrm{DE}}(z)$ tends to approach zero because of the tendency of the effective DE fluid to track the dominant density component [128].

3.5.3   *The covariance of w_{DE}, Σ and μ*

The covariances are computed using eq. (3.38) and are shown, for each class of theories, in figures 3.10, 3.11 and 3.12 of the Appendix B. While it is the covariances that are used in reconstructions, for the purpose of interpreting our results it is more informative to consider the correlation matrices computed using eq. (3.39). They are shown in figures 3.7, 3.8 and 3.9 for the GBD, H_S and Hor models, respectively. For each model, we display the correlations between the bins of the same function as well as the cross-correlations between different functions.

Comparing figures 3.7 and 3.8, one can clearly see that the correlation between Σ and μ and between Σ/μ and w_{DE} is less pronounced in H_S, compared to the GBD case. This is due to the fact that more EFT functions participate in H_S. This trend continues only in part when one compares H_S and Hor in figures 3.8 and 3.9. Namely, the correlation Σ/μ and w_{DE} decreases, as expected, since Hor involves an additional EFT function, γ_3. However, Σ and μ are more correlated in Hor than they are in H_S. This is because γ_3 (equivalently α_T) plays an important role in the stability constraints while being constrained by the condition $\gamma_3(z = 0) = 0$. The net effect of co-varying it with the other functions
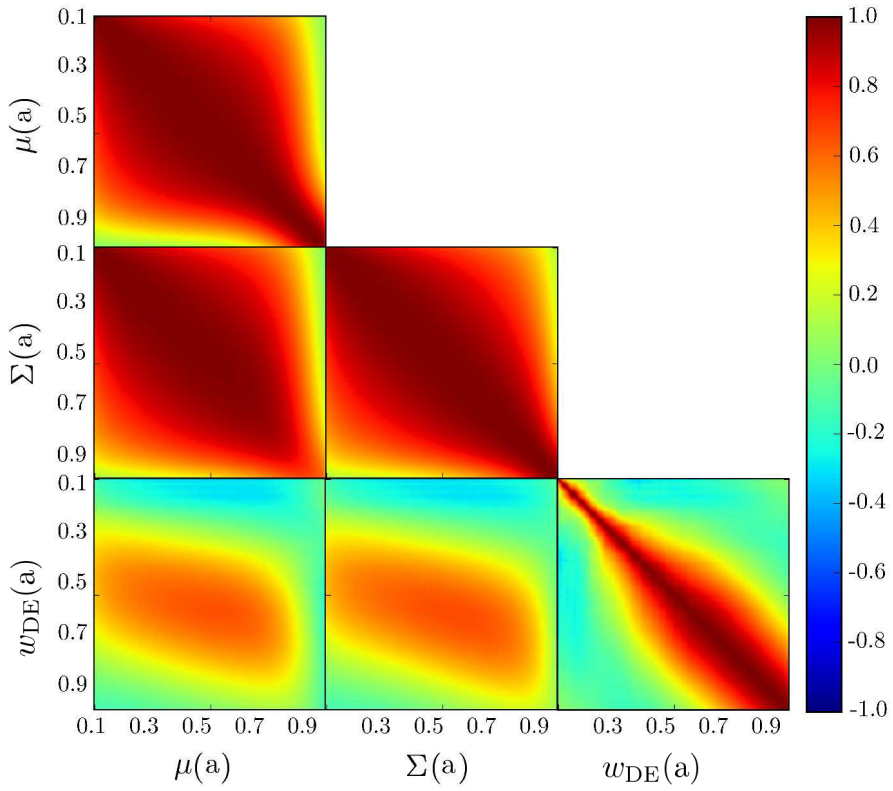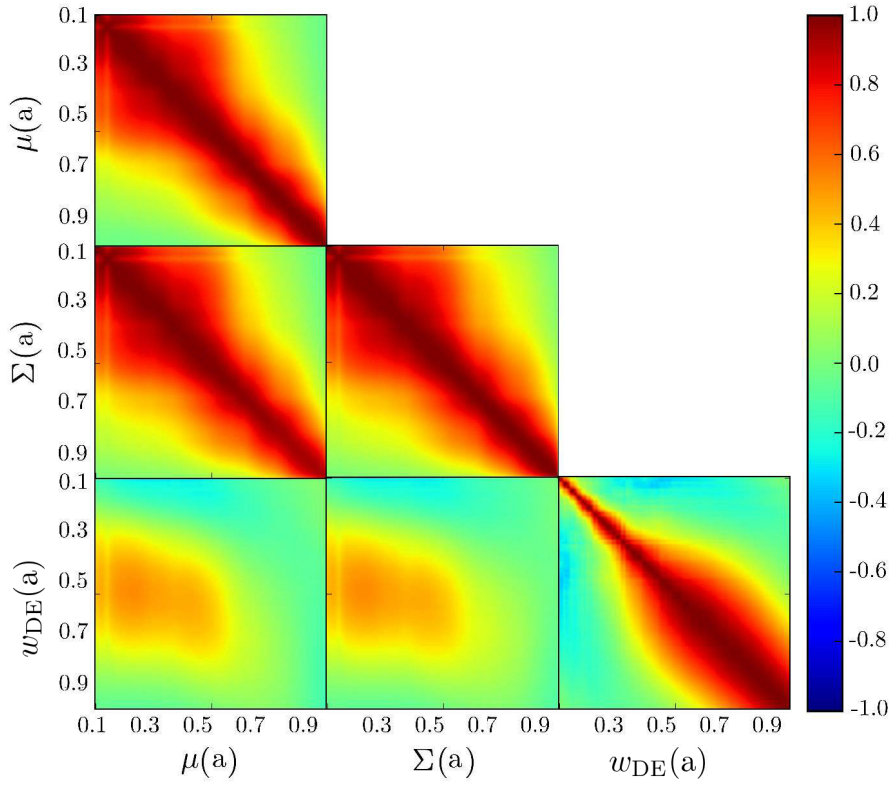
Figure 3.7: Correlation matrices for the GBD models.

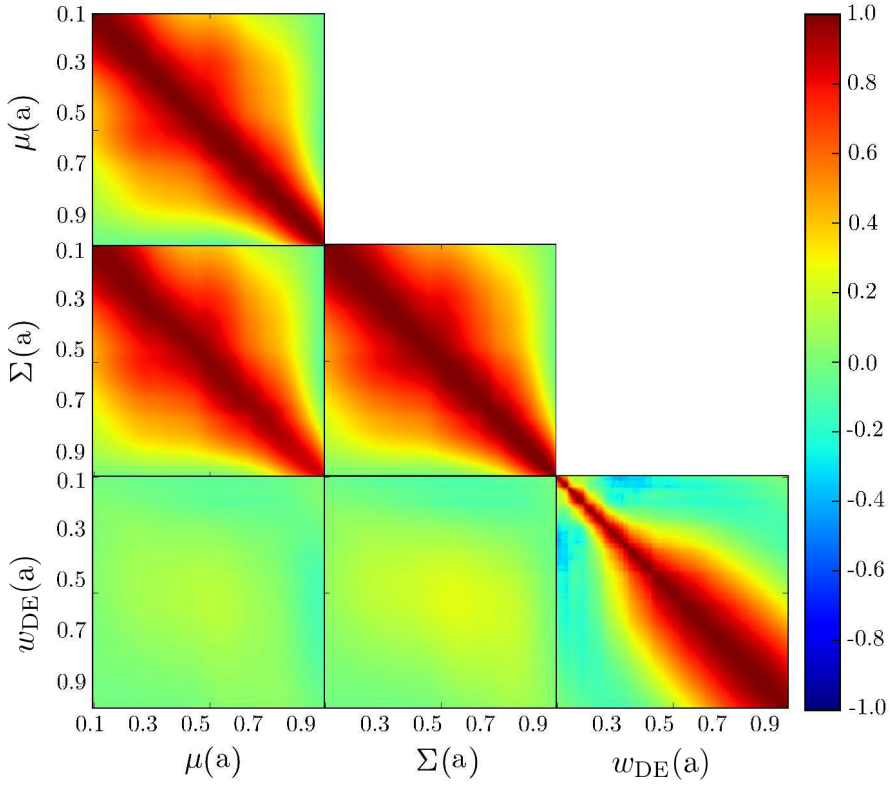**Figure 3.8:** Correlation matrices for the H_S models.

Figure 3.9: Correlation matrices for the Hor models.

is to increase the level of correlation. To check this last point, we ran the same sampling without imposing any stability filter and found that the correlation between Σ and μ decreases as expected when γ_3 is co-varied.

We note that, generally, the correlation between Σ and μ is always significant, as also discussed in [81, 117]. This implies that, when constraining them within the framework of scalar-tensor theories, it does not make sense to fit these two functions to data independently. On the contrary, the cross correlation between Σ and μ and w_{DE} changes visibly for different classes of models. It is strong (up to 60%) in the GBD case: the two non-zero EFT functions, Ω and Λ, participate in the evolution of both the background and linear perturbations. For H_S and Hor, in which the second order EFT functions γ_i affect *only* the perturbations, this cross-correlation decreases. It is weak but still visible for H_S, and completely vanishes in for Hor.

3.5.4 *Analytical forms of correlation functions*

In order to better interpret the numerically found correlation matrices, we fit them with simple analytical expressions. In addition to providing insight into the time scaling of the correlations, they give a readily usable recipe for building correlation priors for practical applications [127, 129, 130] when the numerically found covariances may not be available.

Following the procedures of [128] we use the generalized CPZ parametrization [122] given by

$$\mathcal{C}(x,y) = \frac{1}{1 + (|x - y|/\xi)^n}\,,\tag{3.42}$$

as well as other functional forms used in [128] that, as we found, did not provide a better fit. We let the time coordinate, x and y, be either the scale factor or $\ln a$. We select the best fit analytical form for the correlation by varying the exponent n and the correlation length ξ and

The best fit forms describing the correlations

	μ	Σ
GBD	$\left(1 + (|\delta a| \, /0.65)^{2.25}\right)^{-1}$	$\left(1 + (|\delta a| \, /0.7)^{2.2}\right)^{-1}$
H_S	$\left(1 + (|\delta a| \, /0.32)^{1.72}\right)^{-1}$	$\left(1 + (|\delta a| \, /0.35)^{1.67}\right)^{-1}$
Hor	$\left(1 + (|\delta a| \, /0.31)^{1.74}\right)^{-1}$	$\left(1 + (|\delta a| \, /0.38)^{1.7}\right)^{-1}$

	w_{DE}
GBD	$\left(1 + (|\delta \ln a| \, /0.29)^{3}\right)^{-1}$
H_S	$\left(1 + (|\delta \ln a| \, /0.3)^{2.9}\right)^{-1}$
Hor	$\left(1 + (|\delta \ln a| \, /0.3)^{2.9}\right)^{-1}$

Table 3.2: The best fit analytical expressions of correlations of μ, Σ and w_{DE} for the three classes of models. For Σ and μ, the correlations depend on $|a - a'|$, while for w_{DE} they scale with $|\ln a - \ln a'|$, for the reasons explained in Sec. 3.5.4.

minimizing the χ^2. The CPZ form (3.42), which happens to capture the features of our numerically found correlation matrices quite well, was designed to act as a low-pass Wiener filter. Namely, it assumes no prior correlation on widely separated time scales ($|x - y| > \xi$), allowing any slow, low-frequency, variations of the functions to pass through unbiased. On shorted time scales ($|x - y| < \xi$), however, any high-frequency variations will be suppressed, as the prior implies strong correlations between the neighbouring bins.

In the application of the correlation priors, the most important feature is their behaviour around the peak of the prior distribution. For this reason, for correlations of Σ and μ, we do not attempt to model the tails, and only fit the correlation $\mathcal{C}$ in the range $[x_p - \Delta x, x_p + \Delta x]$, where x_p corresponds to the peak of the correlation at each value of y and Δx was chosen to be $\Delta a = 0.2$. We do not fit the cross-correlations between different functions. In the case of Σ and μ, it is clear from figures 3.7, 3.8 and 3.9 that their cross-correlations will have roughly the same functional form as the correlations. On the other hand, the cross-correlation between w_{DE} and Σ/μ is only relatively strong for GBD and can probably be ignored in practical applications when the numerically found covariances (shown in the Appendix 3.9) are not available.

The best fit functional forms of the correlations are shown in Table 3.2. We notice that the time scaling for Σ and μ correlations is in terms of a, while the correlations for w_{DE} scale with $\ln a$. This difference in scaling can be explained by observing that our sampling of the EFT functions is more or less uniform in a. The correlations of Σ and μ retain the uniformity in a because they directly depend on the EFT functions. In the case of w_{DE}, however, the non-minimal coupling of the scalar field leads to a tracking behaviour of the effective DE fluid, with its evolution dependent on the matter density $\rho_m \propto a^{-3}$. With the effective DE scaling as a power law of a, the correlations of its equation of state scale with $\ln a$. This scaling was also observed in [128],

where it was also shown that for the minimally coupled scalar field, *i.e.* the quintessence, the correlations scale as *a*, consistent with the above explanation.

In the case of w_{DE} correlations, the CPZ parameters ξ and n are approximately the same in the three classes of models, at $\xi \approx 0.3$ and $n \approx 3$. This is because the sampling of the background evolution depends mostly on the EFT functions Ω and Λ in all three cases, and only indirectly depends on the γ_i through the effect of stability conditions on model selection.

For Σ and μ correlations, there is a clear trend for correlations to become shorter range as one goes from GBD to H_S and Hor. The correlation length is $\xi = 0.65$ for GBD, but $\xi \approx 0.3$ for H_S and Hor. There is also a small change in the exponent from $n \approx 2.2$ to $n \approx 1.7$. The fact that the best fit forms of the correlation functions for H_S and Hor are so similar suggests that the minor visible differences between figures 3.8 and 3.9 concern mostly the tails of the correlation matrix, whereas our fits were performed near the peaks.

3.6 DISCUSSION

We studied the statistical distributions of the effective DE equation of state w_{DE} and the phenomenological functions Σ and μ within the Horndeski class of scalar-tensor theories. In order to do so, we worked within the unifying EFT framework and generated large ensembles of statistically independent models using Monte Carlo methods. Such models were filtered in order to pass the no-ghost and no-gradient instability constraints, as well as a set of weak observational constraints.

We have considered three types of Horndeski theories summarized in Table 3.4: the Generalized Brans-Dicke (GBD) models, *i.e.* models with a canonical form of the scalar field kinetic energy term, the H_S class of models, with the unchanged speed of gravitational waves, and the full class of Horndeski models with the speed of gravity constrained

to be the same as the speed of light at present epoch, to comply with the strict bound on the gravitational wave speed at $z < 0.01$ from GW170817 and GRB170817A [61–63].

For each model, we computed Σ and μ by numerically solving the exact equations for cosmological perturbations, and also by using the analytical expressions of Σ and μ derived under the QSA. This allowed us to check the validity range of the quasi static approximation (QSA), as well as the validity of the conjecture made in [117] that $(\Sigma - 1)(\mu - 1) \geq 0$ in viable Horndeski theories.

We find that the QSA holds really well at small and intermediate scales, but breaks down at $k \lesssim 0.001$ h/Mpc. This happens despite the fact that the Fourier modes in question are still well-within the scalar field's sound horizon. Instead, it is due to the time-derivatives of the metric and the scalar field perturbations, which are neglected under the QSA, becoming comparable to the spatial derivatives.

We find that the $(\Sigma - 1)(\mu - 1) \geq 0$ conjecture holds very well for the GBD models. It also holds very well for the other two classes of models within the QSA, but the exact calculations show that about 10% of H_S and Horndeski models violate the conjecture at $k = 0.001$ h/Mpc, with $\Sigma > 1$ and $\mu < 1$.

We analytically examined the conditions under which $(\Sigma - 1)(\mu - 1) \geq 0$ can be violated, separately considering the QS expressions for Σ and μ on the super-Compton and sub-Compton limits. We identified the important role played by the no ghost and no gradient instability conditions in preventing values in the $\Sigma > 1$ and $\mu < 1$ range. We have also highlighted the importance of the constraints on the variation of the gravitational coupling in ensuring the $(\Sigma - 1)(\mu - 1) \geq 0$ trend. Since the variation of the gravitational coupling affects the background expansion history, constraints on the latter contribute to restricting the range of Σ and μ values. This effect was not included in an earlier study of correlations between Σ and μ [165] that was based on a framework in which the expansion history was assumed to be known independently

from the functions controlling the evolution of perturbations. This shows that, when searching for signatures of MG, the expansion history should be co-varied with Σ and μ aided by weak theoretical priors, which we then derived in the form of joint covariance matrices for binned w_{DE}, Σ and μ. These matrices can be projected onto priors on parameters of any specific parametrization of these functions.

We spotted some notable differences in both the mean values and the covariances of w_{DE}, Σ and μ between the different classes of models depending on which constraints are imposed. For instance, we found that restrictions on the variation of the conformal coupling Ω directly impact the mean values of Σ and μ, and less directly the shape of w_{DE}. Furthermore, we found that the latter condition, as well as the constraints on the speed of gravity, have a bigger impact than the physical viability conditions built in EFTCAMB.

We have identified simple analytical forms for the correlation functions, describing the correlations of w_{DE}, Σ and μ at different redshifts, by fitting the CPZ parametrization (3.42) to our numerical results. We noticed that in all the classes of models that we considered, the correlations of Σ and μ scale with $|a - a'|$, while for w_{DE} they scale with $|\ln a - \ln a'|$. These analytical forms can be useful in practical applications of the Bayesian reconstruction method [126].

Our study demonstrates the benefits and the complementarity of different frameworks for testing scalar-tensor alternatives to GR. Phenomenological functions such as Σ and μ are closely related to observations and can be directly fit to data using simple parameterizations. However, there is no guarantee that their best fit values would be consistent with theory. On the other hand, fitting the EFT functions of (1.62) or the Unified functions of (1.64) directly to data is not practical, as there are many degeneracies and the outcome strongly depends on the assumed functional form.

Instead, we used the EFT framework to derive theoretical priors that can be used to perform a joint non-parametric reconstruction of w_{DE},

Σ and μ from data similarly to the case done for w_{DE} in [127, 129]. Introducing such joint correlation priors in the analysis will be essential in order to get significant constraints on the time evolution of the phenomenological functions within the context of scalar-tensor theories, while avoiding biasing the results by assuming specific functional forms. Such unbiased reconstructions would either constrain ΛCDM further, or perhaps point us towards an alternative theory of gravity.

3.7 ACKNOWLEDGMENTS

For the work presented in this chapter we thank Luis Perenon and Federico Piazza for useful discussions.

3.8 APPENDIX A: RELEVANT EQUATIONS

Under the QSA, the equations of motion for perturbations in Horndeski theories can be written as [43]

$$A_1 \frac{k^2}{a^2} \Phi + A_2 \frac{k^2}{a^2} \pi = -\rho \Delta, \tag{3.43}$$

$$B_1 \Psi + \Phi + B_3 \pi = 0, \tag{3.44}$$

$$C_1 \frac{k^2}{a^2} \Phi + C_2 \frac{k^2}{a^2} \Psi + \left(C_3 \frac{k^2}{a^2} + C_\pi \right) \pi = 0, \tag{3.45}$$

where

$$A_1 = 2(m_0^2\Omega + \bar{M}_2^2),$$
$$A_2 = -m_0^2\dot{\Omega} - \bar{M}_1^3,$$
$$B_1 = -\frac{m_0^2\Omega + \bar{M}_2^2}{m_0^2\Omega},$$
$$B_3 = -\frac{m_0^2\dot{\Omega} + (H + \partial_t)\bar{M}_2^2}{m_0^2\Omega},$$
$$C_1 = m_0^2\dot{\Omega} + (H + \partial_t)\bar{M}_2^2,$$
$$C_2 = -\frac{1}{2}(m_0^2\dot{\Omega} + \bar{M}_1^3),$$
$$C_3 = c - \frac{1}{2}(H + \partial_t)\bar{M}_1^3 + (H^2 + \dot{H} + H\partial_t)\bar{M}_2^2,$$
$$C_\pi = \frac{m_0^2}{4}\dot{\Omega}\dot{R}^{(0)} - 3c\dot{H} + \frac{3}{2}(3H\dot{H} + \dot{H}\partial_t + \ddot{H})\bar{M}_1^3$$
$$+ 3\dot{H}^2\bar{M}_2^2. \tag{3.46}$$

The phenomenological functions μ and Σ can be written as

$$4\pi G\mu = \frac{\mu}{2m_0^2} = \frac{f_1 + f_2\, a^2/k^2}{f_3 + f_4\, a^2/k^2}, \tag{3.47}$$

$$8\pi G\Sigma = \frac{\Sigma}{m_0^2} = \frac{f_1 + f_5 + (f_2 + f_6)a^2/k^2}{f_3 + f_4\, a^2/k^2}, \tag{3.48}$$

where

$$f_1 = C_3 - C_1 B_3,$$
$$f_2 = C_\pi,$$
$$f_3 = A_1(B_3 C_2 - B_1 C_3) + A_2(B_1 C_1 - C_2),$$
$$f_4 = -A_1 B_1 C_\pi,$$
$$f_5 = B_3 C_2 - B_1 C_3,$$
$$f_6 = -B_1 C_\pi. \tag{3.49}$$

The functions appearing in the "Unified" action (1.64) are related to the functions appearing in the EFT action (1.62) via [47]

$$M_*^2 = m_0^2 \Omega + \bar{M}_2^2, \tag{3.50}$$

$$H M_*^2 \alpha_M = m_0^2 \dot{\Omega} + \dot{\bar{M}}_2^2, \tag{3.51}$$

$$M_*^2 \alpha_T = -\bar{M}_2^2, \tag{3.52}$$

$$H M_*^2 \alpha_B = -m_0^2 \dot{\Omega} - \bar{M}_1^3, \tag{3.53}$$

$$H^2 M_*^2 \alpha_K = 2c + 4M_2^4. \tag{3.54}$$

$$\tag{3.55}$$

These are related to the functions in the original Horndeski Lagrangian (1.59) via [47]

$$M_*^2 = 2[G_4 - 2XG_{4X} + XG_{5\phi} - \dot{\phi} H X G_{5X}], \tag{3.56}$$

$$H M_*^2 \alpha_M = \frac{dM_*^2}{dt}, \tag{3.57}$$

$$M_*^2 \alpha_T = 2X[2G_{4X} - 2G_{5\phi} - (\ddot{\phi} - H\dot{\phi})G_{5X}], \tag{3.58}$$

$$\begin{aligned} H M_*^2 \alpha_B &= 2\dot{\phi}[XG_{3X} - G_{4\phi} - 2XG_{4\phi X}] \\ &+ 8XH(G_{4X} + 2XG_{4XX} - G_{5\phi} - XG_{5\phi X}) \\ &+ 2\dot{\phi} X H^2 [3G_{5X} + 2XG_{5XX}], \end{aligned} \tag{3.59}$$

$$\begin{aligned} H M_*^2 \alpha_K &= 2X[K_X + 2XK_{XX} - 2G_{3\phi} - 2XG_{3\phi X}] \\ &+ 12\dot{\phi} X H [G_{3X} + XG_{3XX} - 3G_{4\phi X} - 2XG_{4\phi XX}] \\ &+ 12XH^2 [G_{4X} + 8XG_{4XX} + 4X^2 G_{4XXX}] \\ &- 12XH^2 [G_{5\phi} + 5XG_{5\phi X} + 2X^2 G_{5\phi XX}] \\ &+ 4\dot{\phi} X H^3 [3G_{5X} + 7XG_{5XX} + 2X^2 G_{5XXX}]. \end{aligned} \tag{3.60}$$

The speed of sound of the scalar field perturbations is given by

$$\begin{aligned} c_s^2 &= \frac{2}{\alpha} \Big[\Big(1 - \frac{\alpha_B}{2}\Big) \Big(\alpha_M - \alpha_T + \frac{\alpha_B}{2}(1 + \alpha_T) - \frac{\dot{H}}{H^2}\Big) \\ &+ \frac{\dot{\alpha}_B}{2H} - \frac{\rho_m + P_m}{2M_*^2 H^2} \Big], \end{aligned} \tag{3.61}$$

where $\alpha = \alpha_K + 3\alpha_B^2/2$.

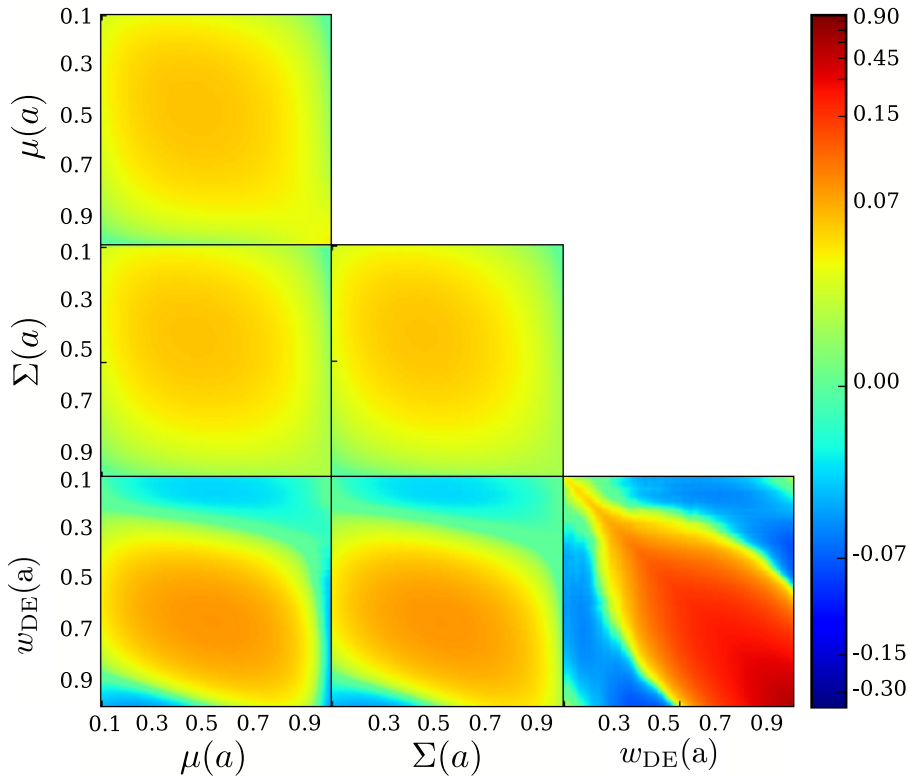## 3.9 APPENDIX B: COVARIANCE MATRICES

Figure 3.10: Covariance matrices for the GBD class of models.

In practical applications of the Bayesian reconstruction method [126], one needs theoretical priors in the form of joint covariances of $w_{\mathrm{DE}}(a)$, $\Sigma(a)$ and $\mu(a)$. These are shown in figures 3.10, 3.11 and 3.12 for the three classes of models considered in this chapter.
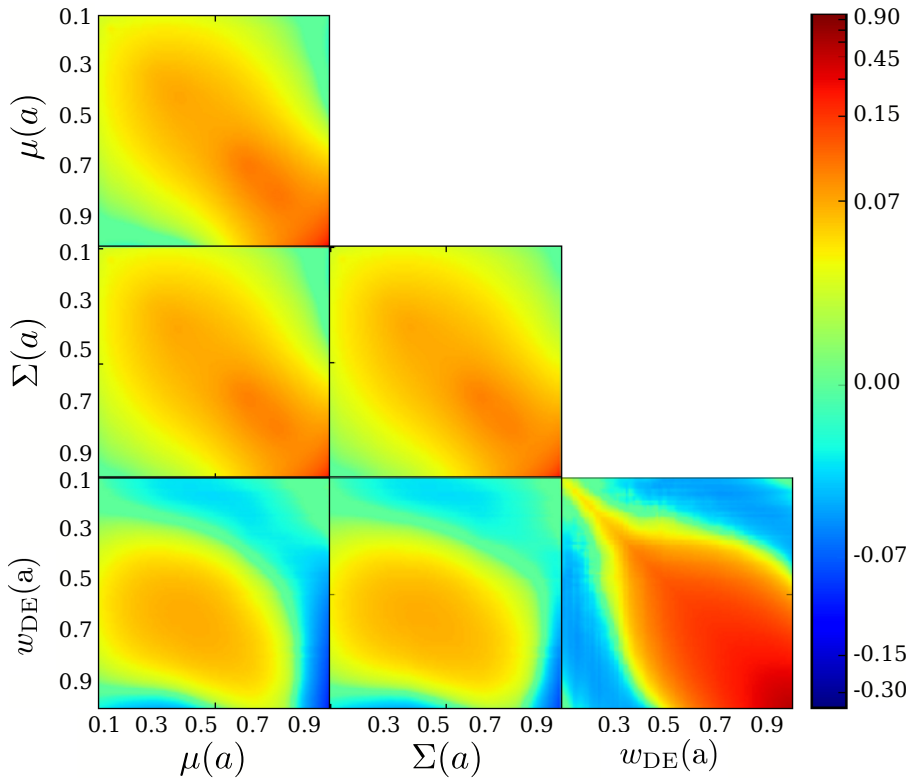
Figure 3.11: Covariance matrices for the H_S class of models.

One can see that the prior variance in $w_{DE}(a)$ is smaller at higher redshifts and becomes larger towards $a = 1$. This is because at higher redshifts, the effective DE tends to track the matter density, hence its equation of state is quite robustly close to zero. On the other hand, at lower redshifts, the effective DE fluid can develop its own independent dynamics as the matter density subsides, and there is more variation of possible $w_{DE}(a)$ histories within the ensemble.

The variances of Σ and μ do not show a strong dependence on redshift, which is a reflection of the approximately uniform sampling
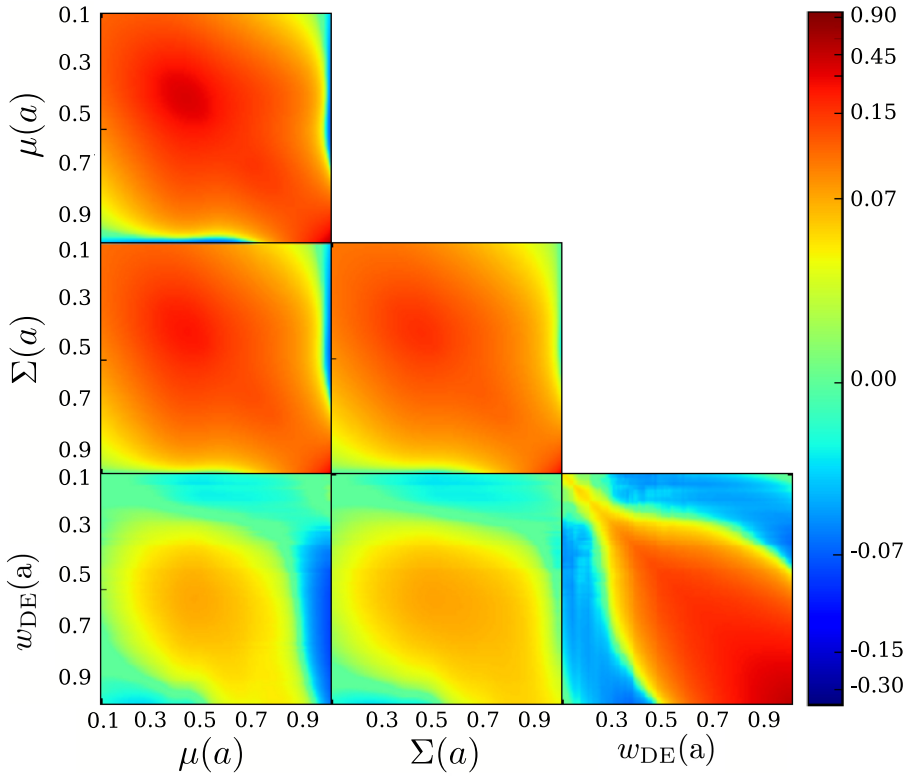
Figure 3.12: Covariance matrices for the Hor class of models.

of the EFT functions in a. The variances increase as one goes from GBD to H_S to Hor, as expected, since the latter have a larger number of varied EFT functions that results in a larger scatter of Σ and μ values.